International Journal of Solids and Structures 259 (2022) 112025

Contents lists available at ScienceDirect

International Journal of Solids and Structures

journal homepage: www.elsevier.com/locate/ijsolstr

Characterization of power-law constitutive relationship of nickel-based single crystal superalloys under different loading rates by nanoindentation with different types of indenters

Xinkuo Ji [a], Gesheng Xiao [a,b,*], Pin Lu [a], Xin Hao [b], Xueling Fan [a,*]

[a] Joint Research Center for Extreme Environment and Protection Technology, State Key Laboratory for Strength and Vibration of Mechanical Structures, School of Aerospace Engineering, Xi'an Jiaotong University, Xi'an 710049, China
[b] Institute of Applied Mechanics, College of Mechanical and Vehicle Engineering, Taiyuan University of Technology, Taiyuan 030024, China

ARTICLE INFO

Keywords:
Nanoindentation
Loading rate
Power-law constitutive
Indentation size effect

ABSTRACT

This work attempts to explore a method to characterize the effect of loading rate on the power-law constitutive parameters of nickel-based single crystal superalloys (NBSX) by nanoindentation, which avoids the influence of indentation sinking-in or piling-up and indentation size effects. Specifically, combing the reduced modulus obtained from a cylindrical flat punch indentation test with the indentation contact stiffness obtained from two pyramidal indentation tests with different equivalent half cone angles, the actual indentation projected contact area of two pyramidal indenters can be acquired. Based on the actual projected contact area and the intrinsic hardness results calculated by Nix-Gao model, the corrected indentation load-depth curves from two pyramidal indenters are constructed. The elastic modulus can be known from the reduced modulus in advance, and then according to the equivalent half cone angle of the pyramidal indenters and the corrected indentation load-depth curves, the representative strain and stress of two pyramidal indenters are obtained, respectively. The power-law constitutive parameters of NBSX along [001] orientation under different loading rates are accomplished by inverse analyses of the representative stress and strain of two pyramidal indenters, and verified by the test results of a pyramidal indenter with another equivalent half cone angle. Results demonstrate the effectiveness of the explored method.

1. Introduction

As an excellent high temperature metal material, nickel-based single crystal superalloys (NBSX) have been selected as substrate alloys for aeroengine turbine blades (Reed et al., 2009; Tsukada et al., 2011; Xiong et al., 2015). Compared with traditional superalloys, the internal grain boundaries of NBSX are eliminated, and its microstructure is composed of matrix phase (γ phase) and strengthening phase (γ' phase), which with a volume fraction of ~ 70 % embedded in matrix phase. It is this two-phase microstructure that makes NBSX having a series of complex deformation mechanisms, and excellent mechanical properties, corrosion resistance and oxidation resistance (Liu et al., 2020; Durst and Göken, 2004; Salehi et al., 2012; Zhang et al., 2020). With the increase of thrust weight ratio of aeroengine and gas temperature in the front of turbine, thermal barrier coating and gas film pore structure are applied to turbine blades for cooling and protection, and turbine blades undergo complex loading conditions in service (Sun et al., 2020). Therefore, it is significant to effectively characterize the mechanical properties of NBSX (Zhang et al., 2015; Ji et al., 2022).

As an advanced material surface contact mechanical property testing technology, nanoindentation has been extensively used in characterizing the mechanical properties of thin films and substrate alloys (Xiao et al., 2021; Xiao et al., 2017; Yu et al., 2021). In previous works, nanoindentation was used to study the creep properties, and the crystal orientation or temperature effect on the mechanical response of NBSX (Xu et al., 2008; Han et al., 2020; Sawant and Tin, 2008). It is rarely involved in exploring the power-law constitutive relationship of NBSX along the [001] orientation, which is the main load bearing orientation of NBSX.

During nanoindentation, the test results of indentation hardness and

* Corresponding authors at: Joint Research Center for Extreme Environment and Protection Technology, State Key Laboratory for Strength and Vibration of Mechanical Structures, School of Aerospace Engineering, Xi'an Jiaotong University, Xi'an 710049, China (G. Xiao).
E-mail addresses: xiaogs@xjtu.edu.cn (G. Xiao), fanxueling@mail.xjtu.edu.cn (X. Fan).

https://doi.org/10.1016/j.ijsolstr.2022.112025
Received 13 June 2022; Received in revised form 25 October 2022; Accepted 3 November 2022
Available online 8 November 2022

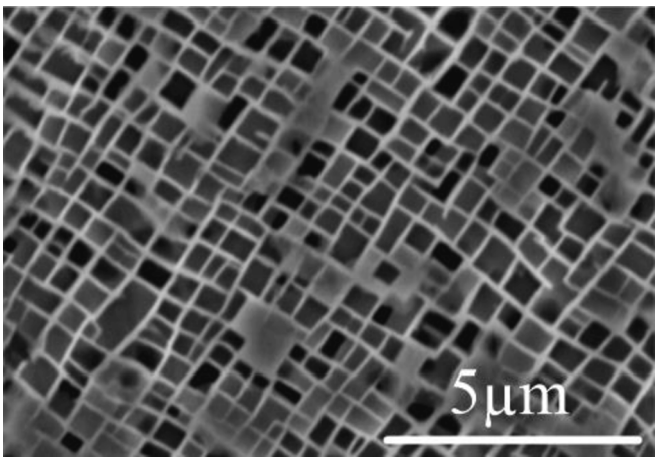

Fig. 1. The microstructure of DD6 NBSX along [001] orientation.

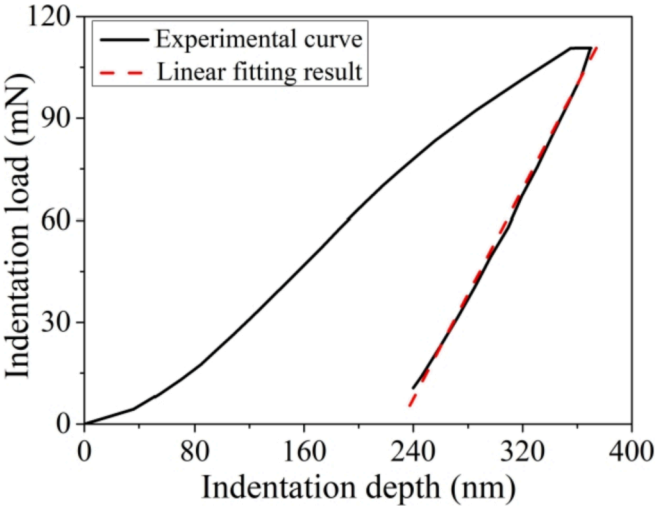

Fig. 2. The result of indentation test with a cylindrical flat punch indenter.

elastic modulus depend on the precision of the indentation projected contact area. The indentation sinking-in effect occurs when the plastic deformation of tested material is accommodated by the surrounding elastic deformation space, on the opposite, the piling-up effect occurs (Iracheta et al., 2019). Obviously, the occurrence of indentation sinking-in or piling-up effect will affect the accuracy of test results. Various works were carried out to study the relationship between sinking-in or piling-up effect and the mechanical response of tested material (Taljat and Pharr, 2004; Cheng and Cheng, 1998; Bolshakov and Pharr, 1998). Furthermore, Oliver and Pharr (Oliver and Pharr, 1992) established a model for calculating the actual projected contact area without considering the piling-up effect. A method was given by N'jock et al. (N'Jock et al., 2015) to approximately calculate the actual projected contact area when the piling-up effect is dominant. Based on finite-element simulation, Xu et al. (Xu and Agren, 2004) proposed an empirical model for obtaining the actual projected contact area under sinking-in or piling-up effect. In addition, finite element simulation or scanning electron microscope observation can be also used to calculate the actual projected contact area (Chen et al., 2006; Fang et al., 2016).

The results of scaling analyses show that the indentation hardness is a constant value and independent of indentation depth (Cheng and Cheng, 2004). However, during nanoindentation, the value of indentation hardness shows an increasing regime as indentation depth decreases, this phenomenon is termed as indentation size effect (ISE). For the purpose of describing this phenomenon, Fleck et al. (Fleck and Hutchinson, 1997) proposed a strain gradient theory including rotational strain gradient and tensile strain gradient. Shu et al. (Shu and Fleck, 1999) further developed Fleck's work to establish a strain gradient model suitable for crystals. Based on the strain gradient theory, Nix and Gao (Nix and Gao, 1998) established a dislocation model for characterizing the form of indentation hardness variation with indentation depth. However, due to the influence of the indenter tip radius and the storage volume of geometrically necessary dislocations (GNDs), the measured results of indentation hardness will be less than that calculated by Nix-Gao model when the indentation depth is less than 100 nm (Qu et al., 2004; Durst et al., 2005). Huang et al. (Huang et al., 2016) proposed a theoretical model based on the maximum allowable GNDs density to further develop the Nix-Gao model. Duan et al. (Liu

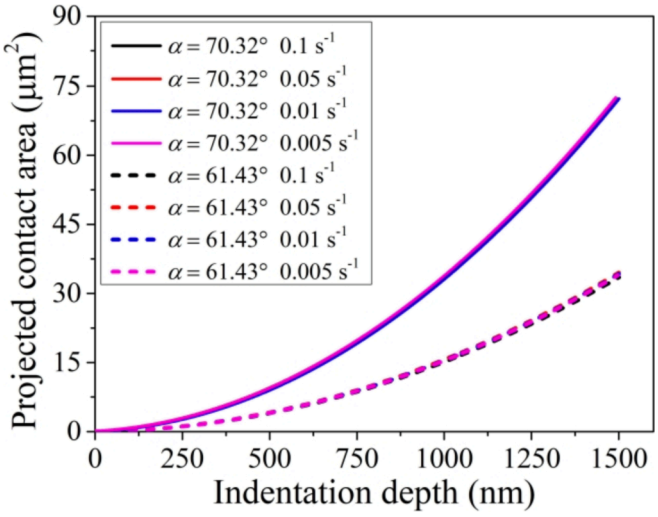

Fig. 4. The actual projected contact area of indentation tests with pyramidal indenters.

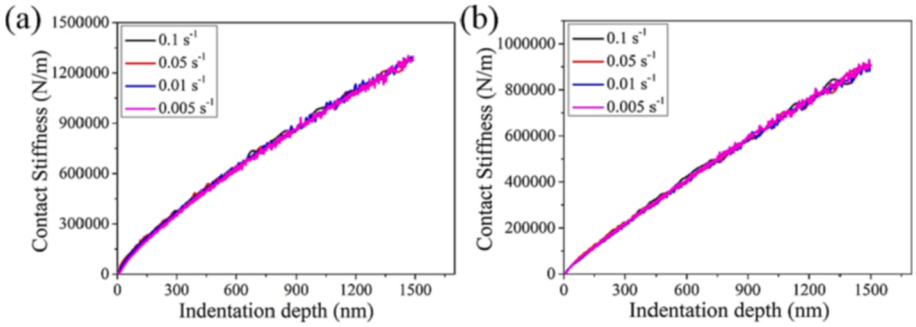

Fig. 3. The contact stiffness results of indentation tests with pyramidal indenters (a) $\alpha = 70.32°$, (b) $\alpha = 61.43°$.

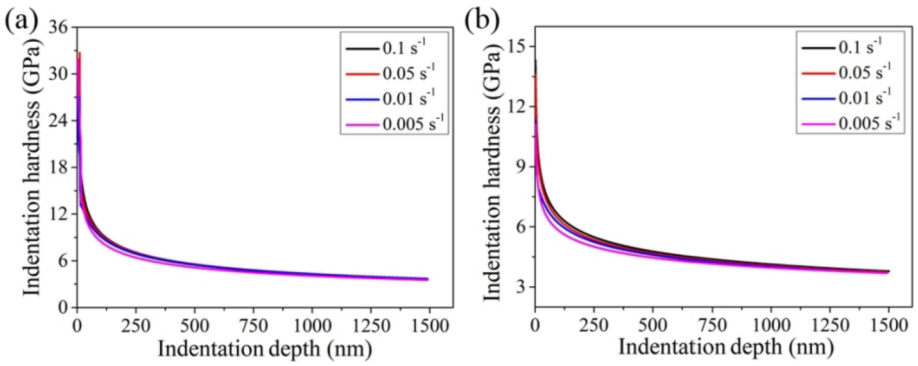

Fig. 5. The indentation hardness results of indentation tests with pyramidal indenters (a) $\alpha = 70.32°$, (b) $\alpha = 61.43°$.

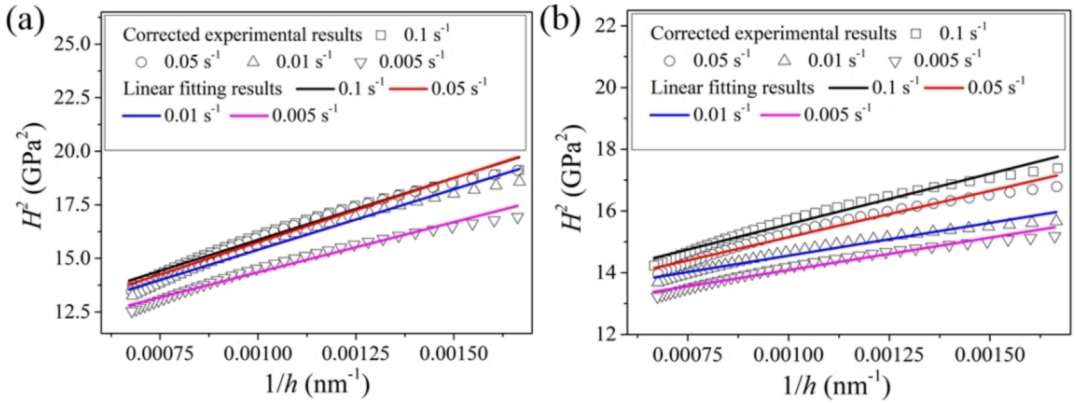

Fig. 6. The H^2-$1/h$ of indentation tests with pyramidal indenters (a) $\alpha = 70.32°$, (b) $\alpha = 61.43°$.

Table 1
The intrinsic hardness results of NBSX.

$\dot{P}/P(s^{-1})$	0.005	0.01	0.05	0.1
H_0 (GPa) $\alpha = 70.32°$	3.100	3.112	3.157	3.174
H_0 (GPa) $\alpha = 61.43°$	3.440	3.451	3.486	3.506

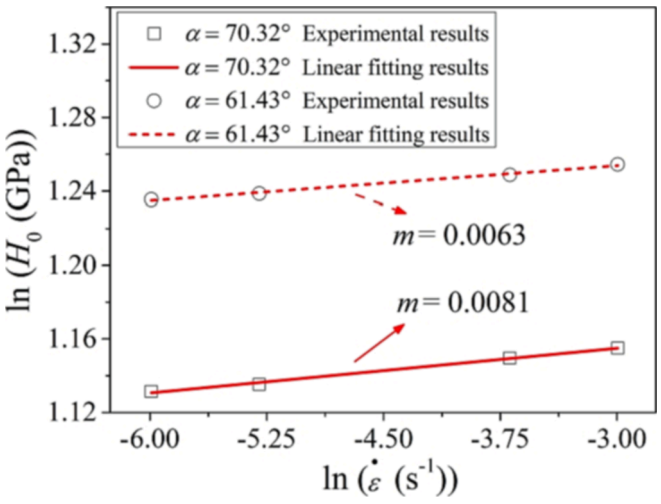

Fig. 7. The ln (H_0) - ln ($\dot{\varepsilon}$) of indentation tests with pyramidal indenters.

et al., 2019) established a modified model considering the influence of elastic deformation to solve the problem of poor prediction by the Nix-Gao model when the indentation depth is small. In addition, dislocation slip and plasticity models were also constructed for exploring the evolution of dislocation structure (Reuber et al., 2014; Po et al., 2019). However, there are few works can comprehensively consider the influence of indentation sinking-in or piling-up effect and ISE on the results of nanoindentation.

In this work, different types of indenters (two pyramidal indenters with different equivalent half cone angles and a cylindrical flat punch indenter) are used to explore the effect of loading rate on the power-law constitutive parameters of NBSX along [001] orientation. Specific calculation procedures are performed on the indentation results based on the indentation contact theory and Nix-Gao model, the actual indentation projected contact area avoiding sinking-in or piling-up effect and indentation load-depth curves without ISE of pyramidal indentations can be obtained. According to the indentation load-depth curves without ISE and Kick's law, the power-law constitutive parameters of NBSX along [001] orientation under different loading rates are calculated based on inverse analyses of the representative stress and strain. This method may be used to effectively characterize the power-law constitutive parameters of metal or alloy material, avoiding the influence of indentation sinking-in or piling-up effect and ISE.

2. Nanoindentation tests

The second-generation NBSX (DD6) of China was taken as the tested material for this work. The [001] crystal oriented NBSX rod was cut into a cube with the length, width and height of 10 mm, 2 mm and 6 mm, respectively, and then it was inlaid with oak powder. The sample surface was gradually polished using various sandpapers from coarse to fine and electrolytic polishing. The microstructure of NBSX along [001] orientation is depicted in Fig. 1.

Nanoindentation tests were carried out on the Nanoindenter G200 (Agilent Technologies), the [001] orientation of NBSX was tested by a

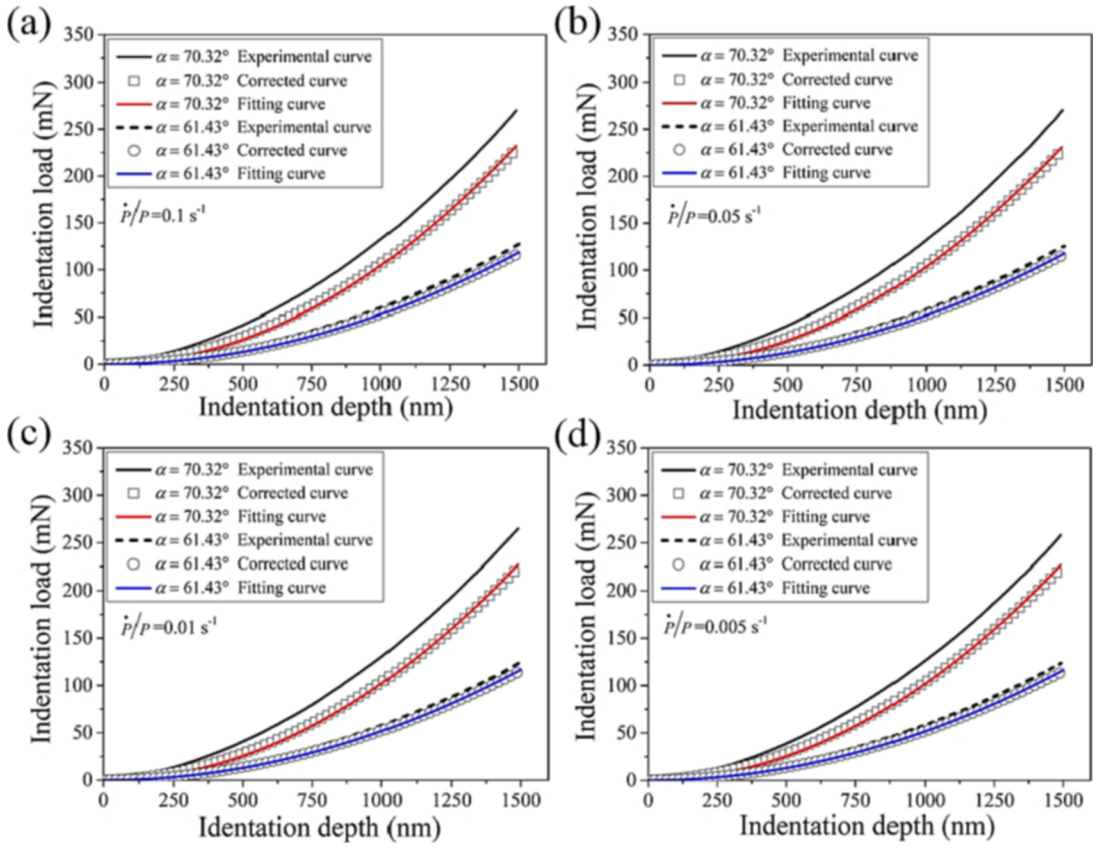

Fig. 8. The indentation load-depth curves of pyramidal indenters.

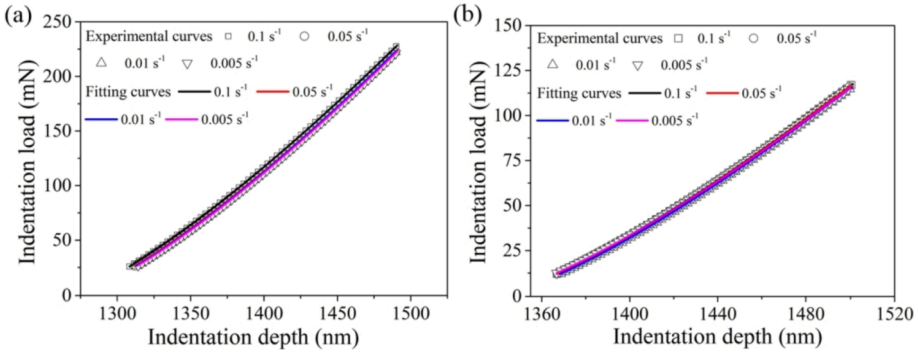

Fig. 9. The corrected indentation unloading curves of pyramidal indenters, (a) $\alpha = 70.32°$, (b) $\alpha = 61.43°$.

cylindrical flat punch indenter with the radius of 2.75 μm. The maximum indentation load was 110 mN, the time of loading, holding and unloading stage were 5 s, 10 s and 2.5 s, respectively.

Two pyramidal indenters with equivalent half cone angle of 70.32° and 61.43° were used to test the [0 0 1] orientation of NBSX by continuous stiffness measurement (CSM), respectively. The maximum indentation depth was 1500 nm. Four loading strain rates ($\dot{P}/P$) of 0.005, 0.01, 0.05 and 0.1 s^{-1} were adopted for the tests, with the indenter unloading in compliance with the normal setting of the nanoindenter. Six parallel tests were conducted for each indentation working condition, and then representative results were obtained.

3. Theoretical analyses

For the unloading elastic recovery curve of nanoindentation, the reduced modulus E_r of tested material can be obtained by the following relationship (Oliver and Pharr, 1992):

$$\frac{dP}{dh} = 2\gamma E_r a \tag{1}$$

where P is indentation load, h is indentation depth, a is indentation contact radius, γ is a constant related to the shape of indenter. For a cylindrical flat punch indenter, γ=1.

The relationship between reduced modulus E_r and elastic modulus E as following:

$$E = \left(1-\nu^2\right) \Big/ \left(\frac{1}{E_r} - \frac{1-\nu_i^2}{E_i}\right) \tag{2}$$

where ν is Poisson's ratio of tested material, $E_i = 1141$ GPa, $\nu_i = 0.07$ are the elastic modulus and Poisson's ratio of the diamond indenter, respectively (Oliver and Pharr, 1992).

For most metallic materials, the following power-law constitutive

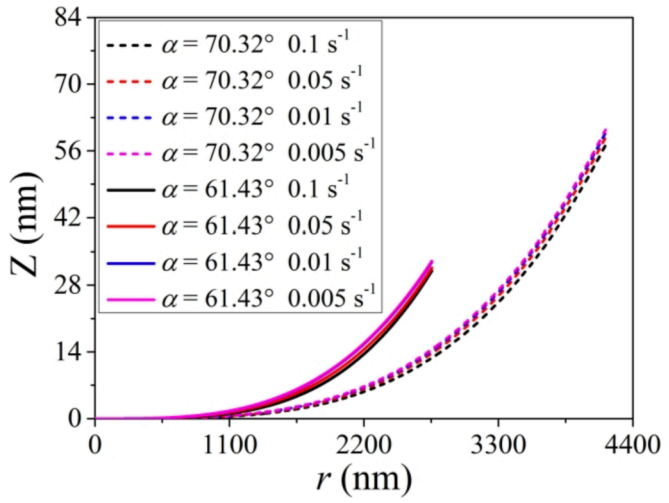

Fig. 10. The effective indenter shape of pyramidal indenters.

Table 2
The calculation results of σ_R and C.

$\dot{P}/P$ (s^{-1})	70.32°			61.43°		
	ε_R	C (GPa)	σ_R(GPa)	ε_R	C (GPa)	σ_R(GPa)
0.005	0.0114	101.959	1.391	0.0174	51.689	1.474
0.01		102.220	1.397		51.832	1.480
0.05		103.515	1.424		52.376	1.500
0.1		104.408	1.440		52.618	1.510

Table 3
The power-law constitutive parameters of NBSX along [0 0 1] orientation.

$\dot{P}/P$ (s^{-1})	σ_y(GPa)	K (GPa)	ε_y	n
0.005	0.931	2.752	0.00669	0.217
0.01	0.939	2.751	0.00675	0.215
0.05	0.999	2.642	0.00718	0.197
0.1	1.043	2.543	0.00750	0.182

relation can well describe the elastic–plastic deformation behavior of materials (Cheng and Cheng, 2004):

$$\sigma = \begin{cases} E\varepsilon, & \varepsilon \leqslant \sigma_y/E \\ K\varepsilon^n, & \varepsilon \geqslant \sigma_y/E \end{cases} \tag{3}$$

where σ and ε are stress and strain, respectively. K, n are strength coefficient and strain hardening exponent, respectively. σ_y is initial yield strength, $\varepsilon_y = \sigma_y/E$ is initial yield strain, and$K = \sigma_y^{1-n}E^n$.

The reduced modulus E_r of tested material can be also expressed as:

$$E_r = \frac{\sqrt{\pi}}{2\beta}\frac{S}{\sqrt{A_c}} \tag{4}$$

where S is indentation contact stiffness, A_c is indentation projected contact area, $\beta = 1.034$ is a constant for the pyramidal indenter (Oliver and Pharr, 1992).

As a dynamic measurement method, CSM can record the contact stiffness of the tested material continuously at the loading stage of an indentation (Oliver and Pethica, 1989). Therefore, combining Eq. (1) with Eq. (4), the actual indentation projected contact area A_c without the influence of sinking-in or piling-up effect can be obtained as:

$$A_c = S^2\pi/4\beta^2E_r^2 \tag{5}$$

According to the definition of indentation hardness H,

$$H = \frac{P}{A_c} \tag{6}$$

Due to the objective existence of indentation strain gradient, the indentation hardness results are affected by ISE. Nix and Gao (Nix and Gao, 1998) developed a model to quantitatively describe the variation of indentation hardness with indentation depth:

$$\frac{H}{H_0} = \sqrt{1 + \frac{h^*}{h}} \tag{7}$$

For the convenience of calculation, Eq. (7) can be transformed into:

$$H^2 = H_0^2 + H_0^2h^*/h \tag{8}$$

where H_0 is the intrinsic hardness without the influence of ISE, h^* is a characteristic length describing the depth dependence of indentation hardness. Obviously, a linear fitting can be performed on the square of indentation hardness and the reciprocal of indentation depth, the intercept result will be the square of intrinsic hardness (H_0^2).

For the CSM mode, $\dot{P}/P$ is a constant, the indentation strain rate $\dot{\varepsilon} = \dot{h}/h$ can be obtained (Xiao et al., 2019):

$$\dot{\varepsilon} = \dot{P}\Big/2P \tag{9}$$

According to scaling analyses, the following relationship can be established (Cheng and Cheng, 2001);

$$H_0 = B\dot{\varepsilon}^m \tag{10}$$

where B is a constant, m is strain-rate sensitivity exponent. Therefore, m can be calculated as:

$$m = \mathrm{d}\ln(H_0)/\mathrm{d}\ln(\dot{\varepsilon}) \tag{11}$$

Based on the results of Eq. (5) and Eq. (8), the indentation load P_a without ISE at loading stage can be obtained by:

$$P_a = H_0A_c \tag{12}$$

For a pyramidal indenter, the indentation load-depth curves at the loading stage can be well described by Kick's law (Oliver and Pharr, 1992):

$$P_a = Ch^2 \tag{13}$$

where C is a constant related to the tested material and the shape of the indenter.

During nanoindentation, it is difficult to obtain the stress and strain of the deformed part directly and accurately. Representative stress and strain were defined for obtaining the mechanical properties of the tested material (Xiao et al., 2021). For a given pyramidal indenter, the corresponding representative stress of tested material can be obtained by dimensionless function, that is (Chen et al., 2007);

$$\frac{C}{\sigma_R} = \prod\left(\frac{\overline{E}}{\sigma_R}\right) \tag{14}$$

where σ_R is the representative stress, $\overline{E} = E/(1-\nu^2)$ is the plane strain modulus.

In order to correct the shortcomings of the previous definition of representative strain, Ogasawara et al. (Ogasawara et al., 2006) redefined the representative strain based on the equi-biaxial loading mode. The representative strain ε_R has a linear relationship with the cotangent value of the equivalent half cone angle of the pyramidal indenter, namely,

$$\varepsilon_R = 0.0319\cot\alpha \tag{15}$$

where α is equivalent half cone angle of the pyramidal indenter. The representative stress σ_R can be calculated by incorporating the elastic

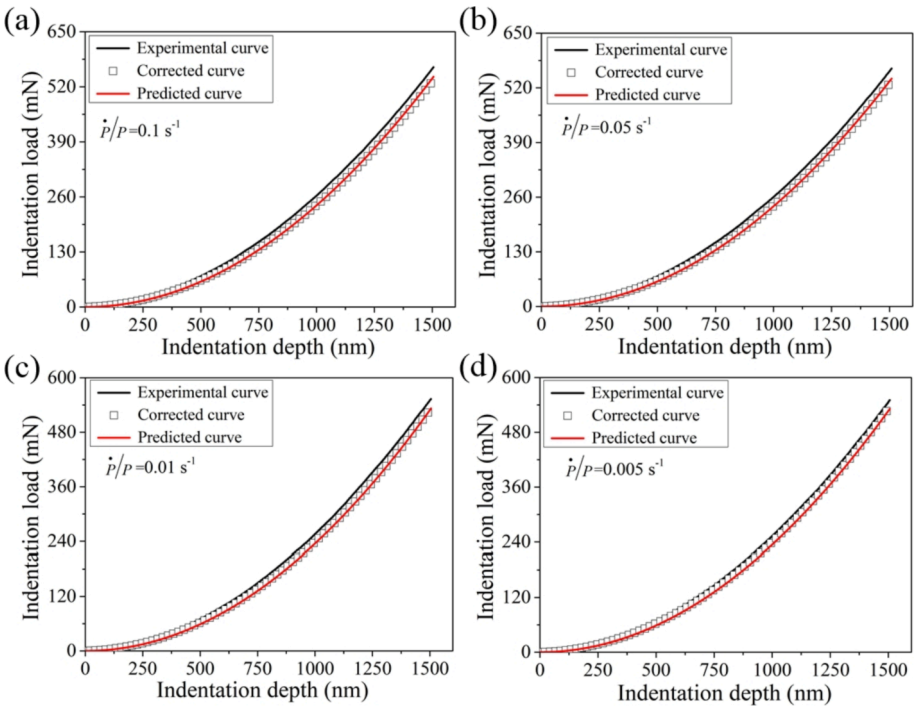

Fig. 11. The indentation load-depth curves and predicted curves of power-law constitutive parameters.

and rigid plastic limit as following (Ogasawara et al., 2006):

$$\sigma_R = m_e C\overline{E}/m_p(m_e\overline{E} - C) \tag{16}$$

where $m_e = 2\chi\tan\alpha/\pi$ and $m_p = 13.2\tan^2\alpha + 6.18\tan\alpha - 8.54$ are elastic and rigid plastic limit, respectively, χ is a correction factor developed by Pharr et al. (Hay et al., 1999).

For a given pyramidal indenter, the σ_R and ε_R obey the following relationship:

$$\sigma_R = K(2\sigma_R/E + 2\varepsilon_R)^n \tag{17}$$

Obviously, K and n of the power-law constitutive relation can be obtained by using two pyramidal indenters with different equivalent half cone angles.

For a pyramidal indenter, the indentation unloading curves can be expressed as (Pharr and Bolshakov, 2002):

$$P = C_u(h - h_r)^u \tag{18}$$

where C_u, u are constants, h_r is residual indentation depth.

For better understanding the complex elastic–plastic deformation behavior under the pyramidal indenter during unloading, the concept of "an effective indenter shape" was introduced (Fischer, 2007);

$$z = Dr^e \tag{19}$$

where z is the vertical distance from the pyramidal indenter to permanently deformed surface, r is the horizontal distance from the symmetry axis of pyramidal indenter. D, e are constants related to the tested material,

$$D = \frac{1}{\sqrt{\pi}}\left[\frac{2E_r}{C_u}\frac{e}{e+1}\left(\frac{\Gamma(e/2+1/2)}{\Gamma(e/2+1)}\right)^{1/e}\right]^e \tag{20}$$

$$e = 1/(u-1) \tag{21}$$

4. Results and discussion

4.1. Test results of the cylindrical flat punch indenter

Since the projected contact area is always equal to the cross-sectional area of the cylindrical flat punch indenter during nanoindentation, as shown in Fig. 2, according to the linear fitting result of the elastic recovery curve at the unloading stage and the radius of the cylindrical flat punch indenter, the reduced modulus of NBSX can be calculated by Eq. (1), which is $E_r = 138.78$ GPa. Furthermore, the elastic modulus of NBSX can be obtained based on Eq. (2), namely $E = 139.10$ GPa.

4.2. Test results of pyramidal indenters

Contact stiffness indicates the ability of NBSX to resist contact deformation, which is not affected by the loading rate, as manifested in Fig. 3. The relationship between contact stiffness and indentation depth is consistent with the linear result of theoretical analyses (Ji et al., 2022; Xiao et al., 2021). The contact stiffness of NBSX measured by the pyramidal indenter with equivalent half cone angle of 70.32° is higher than that measured by the pyramidal indenter with equivalent half cone angle of 61.43°.

According to the results of contact stiffness and reduced modulus, the actual projected contact area at the loading stage can be obtained based on Eq. (5). As exhibited in Fig. 4, since neither the reduced modulus nor the contact stiffness is affected by the loading rate, the actual projected contact area is almost not affected by the loading rate. Upon analyses, as plastic deformation under the indenter is restrained with loading rate (Ji et al., 2022), the projected contact area decreases imperceptibly.

According to the results of actual projected contact area and Eq. (6), the indentation hardness-depth curves can be obtained avoiding the influence of sinking-in or piling-up effect. Fig. 5 exhibits the value of indentation hardness increases monotonically with decreasing indentation depth, this phenomenon is called ISE. For avoiding the surface effect of tested materials and the curvature effect of indenter tip, the intrinsic hardness results of NBSX were obtained by calculating the indentation hardness curves for the indentation depth exceeding 600 nm

(600–1500 nm) based on the Nix-Gao model, as depicted in Fig. 6. Hardness indicates the ability of NBSX to resist hard objects indenting into its surface. With increasing loading rate, the viscoplastic deformation and viscous flow of NBSX are restrained (Ji et al., 2022), and the NBSX under the indenter is hardened. It can be seen from Table 1 that the intrinsic hardness is enhanced with loading rate. Moreover the intrinsic hardness measured by the pyramidal indenter with equivalent half cone angle of 61.43° is higher than that measured by the pyramidal indenter with equivalent half cone angle of 70.32° under the same loading rate. The strain-rate sensitivity exponent m can be calculated based on Eq. (11). Due to the higher dislocation density inside NBSX tested under a pyramidal indenter with smaller equivalent half cone angle, the sensitivity to loading rate is lower (Fan et al., 1845); just as Fig. 7 demonstrating that $m_{\alpha=70.32^\circ} > m_{\alpha=61.43^\circ}$.

The corrected indentation load-depth curves of pyramidal indenters at loading stage can be obtained based on the results of actual projected contact area and intrinsic hardness. Since the ISE is eliminated in the corrected curves, the corrected indentation load is less than the original experimental indentation load, as illustrated in Fig. 8.

4.3. The effective indenter shape of pyramidal indenters

Since the unloading process is mainly elastic recovery, and the effect of plastic deformation can be ignored (Pharr and Bolshakov, 2002), the complete corrected indentation curves were obtained by translating the part of the original unloading curves below the indentation load P_a to connect to the corrected indentation loading curves. The effective indenter shape of pyramidal indenters can be obtained based on the corrected indentation unloading curves (Fig. 9). Fig. 10 displays that the value of Z decreases with loading rate, indicating that with the increase of loading rate, the stress distribution under the indenter becomes more concentrated, and the elastic recovery of NBSX increases.

4.4. The power-law constitutive parameters of NBSX along [001] orientation

As shown in Fig. 8, the loading coefficient C can be obtained by fitting the corrected indentation load-depth curves according to the Kick's law, furthermore, the representative stress σ_R was calculated by incorporating the elastic and rigid plastic limit. The calculation results were summarized in Table 2. Based on the results of representative stress and strain of two pyramidal indenters with different equivalent half cone angles, the power-law constitutive parameters of NBSX along [001] orientation can be obtained. Table 3 exhibits the power-law constitutive parameters of NBSX along [001] orientation under different loading rates.

Since both dislocation density and deformation activation energy in the matrix phase (γ phase) increase with loading rate (Fan et al., 1845; Zhang et al., 2015); Table 3 obviously reveals the correlation between initial yield strength (strain) of NBSX and loading rate is positive. Although the loading rate enhanced the initial yield strength (strain) of NBSX, the plastic properties of NBSX are inhibited. As loading rate increases, the viscoplastic flow becomes smaller for its hysteresis (Salvado et al., 2017), and the plastic deformation of NBSX is more concentrated, that is, the slip and distribution of dislocations are more nonuniform (Fan et al., 1845). In addition, the dislocation slip velocity displays an increasing regime as the loading rate increases, while the stacking fault width shows a decreasing regime, causing the stacking fault energy increasing and more nonuniform plastic deformation of NBSX (Estrin and Kubin, 1986; Curtze and Kuokkala, 2010). Therefore, Table 3 illustrates both K and n decrease with loading rate.

4.5. Verification of the power-law constitutive parameters of NBSX along [001] orientation

In order to verify the power-law constitutive parameters of NBSX along [001] orientation obtained from the above work, a pyramidal indenter with equivalent half cone angle of 78.23° was indented into the NBSX along [001] orientation under the same four different strain rates by CSM. The predicted indentation load-depth curves by forward analyses of the power-law constitutive parameters and the corrected indentation load-depth curves of test results were plotted in Fig. 11. Considering the good agreement between them, it can be concluded that the power-law constitutive parameters of NBSX along [001] orientation obtained from the above work are reliable.

5. Conclusion

In this work, loading rate effect on the power-law constitutive parameters of NBSX along [001] orientation is characterized by nanoindentation tests with different types of indenters. Specific calculation procedures were performed on the indentation test results based on the indentation contact theory and Nix-Gao model, the indentation load-depth curves avoiding the influence of indentation sinking-in or piling-up effect and ISE can be obtained. Furthermore, according to the corrected indentation load-depth curves, the accurate power-law constitutive parameters of NBSX along [001] orientation under different loading rates can be calculated by inverse analyses of the representative stress and strain of two pyramidal indenters. The indentation contact stiffness and actual projected contact area are almost not affected by loading rate. The strain-rate sensitivity exponent m, indentation contact stiffness and actual projected contact area measured by a pyramidal indenter with larger equivalent half cone angle are larger than that measured by a pyramidal indenter with smaller equivalent half cone angle, however, the intrinsic hardness results are just the opposite. The elastic recovery, initial yield strength σ_y, initial yield strain ε_y and intrinsic hardness of NBSX display an increasing regime as the loading rate increases, while strength coefficient K and strain hardening exponent n are just the opposite. The proposed method can be used to effectively characterize the power-law constitutive parameters of metal or alloy material.

Declaration of Competing Interest

The authors declare that they have no known competing financial interests or personal relationships that could have appeared to influence the work reported in this paper.

Data availability

Data will be made available on request.

Acknowledgement

The authors gratefully acknowledge the financial support from the National Science and Technology Major Project (J2019-IV-0003-0070), the National Natural Science Foundation of China (12272249) and China Postdoctoral Science Foundation (2021M702605).

References

Bolshakov, A., Pharr, G.M., 1998. Influences of pile up on the measurement of mechanical properties by load and depth sensing indentation techniques. J. Mater. Res. 13 (4), 1049–1058.
Chen, X., Jin, Y., Karlsson, A.M., 2006. On the determination of residual stress and mechanical properties by indentation. Mater. Sci. Eng., A 416 (1–2), 139–149.
Chen, X., Ogasawara, N., Zhao, M., et al., 2007. On the uniqueness of measuring elastoplastic properties from indentation: The indistinguishable mystical materials. J. Mech. Phys. Solids 55 (8), 1618–1660.
Cheng, Y.T., Cheng, C.M., 1998. Scaling approach to conical indentation in elastic-plastic solids with work hardening. J. Appl. Phys. 84 (3), 1284–1291.
Cheng, Y.T., Cheng, C.M., 2001. Scaling relationships in indentation of power-law creep solids using self-similar indenters. Philos. Mag. Lett. 81 (1), 9–16.
Cheng, Y.T., Cheng, C.M., 2004. Scaling, dimensional analysis, and indentation Measurements. Mater. Sci. Eng.: R: Rep. 44 (4–5), 91–149.

Curtze, S., Kuokkala, V.T., 2010. Dependence of tensile deformation behavior of TWIP steels on stacking fault energy, temperature and strain rate. Acta Mater. 58 (15), 5129–5141.
Durst, K., Backes, B., Göken, M., 2005. Indentation size effect in metallic materials: Correcting for the size of the plastic zone. Scr. Mater. 52 (11), 1093–1097.
Durst, K., Göken, M., 2004. Micromechanical characterization of the influence of rhenium on the mechanical properties in nickel-base superalloys. Mater. Sci. Eng., A 387–389 (15), 312–316.
Estrin, Y., Kubin, L.P., 1986. Local strain hardening and nonuniformity of plastic deformation. Acta Metall. 34 (12), 2455–2464.
Fan, H.D., Wang, Q., El-Awady, J.A., et al., 1845. Strain rate dependency of dislocation plasticity. Nat. Commun. 2021, 12.
Fang, X.F., Li, Y., Wang, D., et al., 2016. Surface evolution at nanoscale during oxidation: A competing mechanism between local curvature effect and stress effect. J. Appl. Phys. 119, 155302.
Fischer, A.C., 2007. Illustrative analysis of load-displacement curves in nanoindentation. J. Mater. Res. 22 (11), 3075–3086.
Fleck, N.A., Hutchinson, J.W., 1997. Strain gradient plasticity. Adv. Appl. Mechan., NewYork: Academic press 33, 295–361.
Han Q N, Rui S S, Qiu W H, et al. Effect of crystal orientation on the indentation behavior of Ni-based single crystal superalloy. Materials Science and Engineering A, 2020, 773 (31): 138893.1−138893.12.
Hay, J.C., Bolshakov, A., Pharr, G.M., 1999. A critical examination of the fundamental relations used in the analysis of nanoindentation data. J. Mater. Res. 14 (06), 2296–2305.
Huang, Y., Zhang, F., Hwang, K.C., et al., 2016. A model of size effects in nano-indentation. J. Mech. Phys. Solids 54 (8), 1668–1686.
Iracheta, O., Bennett, C.J., Sun, W., 2019. A holistic inverse approach based on a multi-objective function optimisation model to recover elastic-plastic properties of materials from the depth-sensing indentation test. J. Mech. Phys. Solids 128, 1–20.
Ji, X.K., Xiao, G.S., Zhao, W., et al., 2022. Loading rate sensitivity of nickel-based single crystal superalloys characterized by nanoindentation. Int. J. Solids Struct. 234–235, 111272.
Liu, W.B., Chen, L.R., Cheng, Y.Y., et al., 2019. Model of nanoindentation size effect incorporating the role of elastic deformation. J. Mech. Phys. Solids 126, 245–255.
Liu, F., Wang, Z.X., Wang, Z., et al., 2020. Evaluating yield strength of Ni-based superalloys via high throughput experiment and machine learning. J. Micromechan. Molecul. Phys. 05, 2050015.
N'Jock, M.Y., Chicot, D., Ndjaka, J.M., et al., 2015. A criterion to identify sinking-in and piling-up in indentation of materials. Int. J. Mech. Sci. 90, 145–150.
Nix, W.D., Gao, H.J., 1998. Indentation size effects in crystalline materials: A law for strain gradient plasticity. J. Mech. Phys. Solids 46 (3), 411–425.
Ogasawara, N., Chiba, N., Chen, X., 2006. Limit analysis-based approach to determine the material plastic properties with conical indentation. J. Mater. Res. 21 (4), 947–957.
Oliver, W. C, Pethica J. B. Method for continuous determination of the elastic stiffness of contact between two bodies. US, US4848141 A. 1989.
Oliver, W.C., Pharr, G.M., 1992. An improved technique for determining hardness and elastic modulus using load and displacement sensing indentation experiments. J. Mater. Res. 7 (6), 1564–1583.
Pharr, G.M., Bolshakov, A., 2002. Understanding nanoindentation unloading curves. J. Mater. Res. 17 (10), 2660–2671.
Po, G., Huang, Y., Ghoniem, N., 2019. A continuum dislocation-based model of wedge microindentation of single crystals. Int. J. Plast. 114, 72–86.
Qu, S., Huang, Y., Nix, W.D., et al., 2004. Indenter tip radius effect on the Nix-Gao relation in micro- and nanoindentation hardness experiments. J. Mater. Res. 19 (11), 3423–3434.
Reed, R.C., Tao, T., Warnken, N., 2009. Alloys-by-design: application to nickel-based single crystal superalloys. Acta Mater. 57 (19), 5898–5913.
Reuber, C., Eisenlohr, P., Roters, F., et al., 2014. Dislocation density distribution around an indent in single-crystalline nickel: Comparing nonlocal crystal plasticity finite-element predictions with experiments. Acta Mater. 71, 333–348.
Salehi, R., Samadi, A., Savadkoohi, M.K., 2012. Influence of etchants on quantitative/qualitative evaluations of the γ′ precipitates in a nickel-base superalloy. Metallogr. Microstruct. Anal. 1, 290–296.
Salvado, F.C., Teixeira-Dias, F., Walley, S.M., et al., 2017. A review on the strain rate dependency of the dynamic viscoplastic response of FCC metals. Prog. Mater Sci. 88, 186–231.
Sawant, A., Tin, S., 2008. High temperature nanoindentation of a Re-bearing single crystal Ni-base superalloy. Scr. Mater. 58 (4), 275–278.
Shu, J.Y., Fleck, N.A., 1999. Strain gradient crystal plasticity: size-dependent deformation of bicrystals. J. Mech. Phys. Solids 47 (2), 297–324.
Sun, F., Fan, X.L., Zhang, T., et al., 2020. Numerical analysis of the influence of pore microstructure on thermal conductivity and Young's modulus of thermal barrier coating. Ceram. Int. 46 (15), 24326–24332.
Taljat, B., Pharr, G.M., 2004. Development of pile-up during spherical indentation of elastic-plastic solids. Int. J. Solids Struct. 41, 3891–3904.
Tsukada, Y., Murata, Y., Koyama, T., et al., 2011. Creep deformation and rafting in nickel-based superalloys simulated by the phase-field method using classical flow and creep theories. Acta Mater. 59 (16), 6378–6386.
Xiao, G.S., Liu, E.Q., Jin, T., et al., 2017. Mechanical properties of cured isotropic conductive adhesive (ICA) under hygrothermal aging investigated by micro-indentation. Int. J. Solids Struct. 122, 81–90.
Xiao, G.S., Yang, X.X., Ji, Q., et al., 2019. Determination of power hardening elastoplastic constitutive relation of metals through indentation tests with plural indenters. Mech. Mater. 138, 103173.
Xiao, G.S., Ma, Y.H., Ji, X.K., et al., 2021. Effective acquisition of elastoplastic and creep parameters of lead-free solder alloy from high-temperature micro-indentation eliminating the size effect. Mech. Mater. 160, 103985.
Xiong, X.H., Quan, D.M., Dai, P.D., et al., 2015. Tensile behavior of nickel-base single-crystal superalloy DD6. Mater. Sci. Eng., A 636 (11), 608–612.
Xu, Z.H., Agren, J., 2004. An analysis of piling-up or sinking-in behaviour of elastic–plastic materials under a sharp indentation. Phil. Mag. 84 (23), 2367–2380.
Xu, B.X., Wang, X.M., Zhao, B., et al., 2008. Study of crystallographic creep parameters of nickel-based single crystal superalloys by indentation method. Mater. Sci. Eng., A 478 (1–2), 187–194.
Yu, Z.J., Lin, Z.Y., Wei, Y.G., 2021. Investigation on cross-scale indentation scaling relationships of elastic-plastic solids. Acta Mech. 232, 1479–1496.
Zhang, D.X., Wen, Z.X., Yue, Z.F., 2015. Effects of strain rate and temperature on mechanical property of nickel-based superalloy GH3230. Rare Metal Mater. Eng. 44 (11), 2601–2606.
Zhang, Z.K., Wen, Z.X., Yue, Z.F., 2020. Nanoindentation study and mechanical property analysis of nickel-based single crystal superalloys. Mater. Res. Express 7 (9), 096509.
Zhang, H.B., Zhang, K.F., Zhou, H.P., et al., 2015. Effect of strain rate on microstructure evolution of a nickel-based superalloy during hot deformation-science direct. Mater. Des. 80 (5), 51–62.